metals

MDPI

Article

Study of the Double-Layer Sintering Process with Stand-Support

Jie Liu [1], Mingshun Zhou [2], Fadeng Wu [3], Hui Zhang [2], Libing Xu [2], Liwei Zhai [2], Wei Gao [1,*] and Qiang Zhong [1]

[1] School of Minerals Processing and Bioengineering, Central South University, Changsha 410083, China; liujie@csu.edu.cn (J.L.); zhongqiang@csu.edu.cn (Q.Z.)
[2] Iron and Steel Research Institute of AnGang Group, Anshan 114009, China; zhoumingshun@ansteel.com.cn (M.Z.); zhanghui@ansteel.com.cn (H.Z.); xulibing@ansteel.com.cn (L.X.); zhailiwei@ansteel.com.cn (L.Z.)
[3] Hunan Shuangsheng Technology Information Consulting Co., Ltd., Changsha 410083, China; csubiowufd@126.com
* Correspondence: gaowei@csu.edu.cn; Tel.: +86-182-7483-5980

Abstract: It has been widely reported that the sintering productivity and sintering bed permeability would be reduced when adopting ultra-deep bed sintering. To solve the aforementioned problems, the double-layer sintering process with stand-support (DLSP-S) is proposed in this research to achieve the sintering of a 1000 mm ultra-deep bed. The results showed that compared with the double-layer sintering process, the DLSP-S improved the yield and productivity of sintering from 64.53% and 1.76 $t \cdot m^{-2} \cdot h^{-1}$ to 66.74% and 2.12 $t \cdot m^{-2} \cdot h^{-1}$, respectively. The research findings showed that the quasi-fines of 5–10 mm were reduced by 2.1% when the stand height increased from 0 mm to 350 mm, which further illustrated the effect of the DLSP-S. During the DLSP-S, the air permeability of the sinter bed was evidently improved and the content of O_2 in the lower layer was enhanced. The present study provides an effective approach to improve the bed permeability and sintering productivity in high-bed sintering.

Keywords: double-layer sintering; stand-support sintering; air permeability; ultra-deep bed sintering

Citation: Liu, J.; Zhou, M.; Wu, F.; Zhang, H.; Xu, L.; Zhai, L.; Gao, W.; Zhong, Q. Study of the Double-Layer Sintering Process with Stand-Support. *Metals* **2022**, *12*, 629. https://doi.org/10.3390/met12040629

Academic Editor: Eric Hug

Received: 31 January 2022
Accepted: 21 March 2022
Published: 6 April 2022

1. Introduction

With the development of iron-making technology and the growth of iron production in China, the volume of blast furnaces has gradually increased. By 2020, there were 32 blast furnaces with more than 5000 m^3 in the world, and nine of them were in China. This puts forward a higher demand for the yield and quality of sintering products, which account for about 75% of the structure of blast furnaces in China [1,2]. To meet this need, the scale of domestic sintering machines has gradually increased in size, which has inevitably led to the increase in the thickness of the sintering bed. Previous research [3–5] reported that in the 1980s, the thickness of the sintering bed was only 300 mm, and now, it has reached 700–800 mm. In recent years, 1000 mm ultra-thick bed sintering has also been reported [6,7]. However, as the thickness of the material layer has increased, the self-accumulating effect has enhanced, which has resulted in the widening of the high-temperature combustion zone and the occurrence of excessive melting phenomenon at the lower layer of the sinter bed [8]. Moreover, the gravity from the upper raw materials or sintered cake would seriously damage the structure of the sinter bed and change the porosity in the middle and lower material layer [9]. The above problems will increase the resistance of air flow through the material layer and reduce the thermal permeability of the ultra-thick material layer, thereby decreasing the quality and yield of the sintering.

Enormous efforts have been devoted to promoting the permeability of the high-bed sintering process. For instance, Zhang et al. [3] proposed a method for the improvement of bed permeability by a strengthened granulation process. The results showed that by strengthening the granulation, the sintering productivity increased by 0.128 $t \cdot m^{-2} \cdot h^{-1}$ when the bed height increased from 700 mm to 900 mm. Gu et al. [6] focused on improving

the permeability in ultra-thick material sintering with a 1000 mm height through the composite agglomeration process. They found that the cold permeability of the sinter bed was promoted by 10% and the productivity of sintering was increased by 0.34 $t \cdot m^{-2} \cdot h^{-1}$ when adding 40 wt.% pelletized feed into the sinter mixture. Currently, some works study the stand-support sintering to improve the air permeability in the lower part of the material bed [10,11]. In 1995, Higuchi et al. [10] first proposed stand-support sintering with a bed height of 750 mm and found that stand-support sintering remarkably decreased the sintering time and increased the sintering productivity by 20%. Zuo et al. [12–14] researched the effect of the height and the area of the stand on the sintering productivity and the tumbler index in a 600 mm bed height. The results showed that after installing stands on trolleys, the fuel consumption and tumbler index dropped by 1.32% and 0.07%, respectively, while the sintering productivity improved by 6.34%. The stand-support sintering technology can effectively improve the permeability of the material layer and alleviate the gravity of the upper part of the material layer to the lower part. However, the relevant studies in the thickness of the material layer were around 700 mm, and less research has focused on ultra-thick material sintering.

The double-layer sintering process (DLSP), which has a two-stage charging and corresponding ignition process in the same grate, can also effectively enhance the bed permeability and sintering productivity [15,16]. In 2015, Ansteel of China carried out a series of industrial experiments of the DLSP [17]. They noted that under the condition that the concentrate proportion ratio exceeded 60%, the total thickness of the material layer can reach higher than 1000 mm, and the output of a single sintering machine was greatly improved. However, there was a decrease in the yield of the sinter product, and the amount of a 5–10 mm quasi-powder grade was increased. Previous research indicated that the DLSP can greatly elevate the sintering productivity. So far, there are few research works into the ultra-thick sintering such as 1000 mm through the DLSP, and the sintering behavior of the DLSP is still unclear.

This study analyzed the issues in the DLSP and developed a double-layer sintering process with stand-support (DLSP-S) to overcome the flaws of poor permeability and low sintering productivity in an ultrathick bed. The influences of the stand height on the sinter quality were researched through sinter pot tests at an ultra-thick bed height of 1000 mm. Then, the bed permeability, flue gas composition, and sintering product properties of the DLSP-S were tested to offer an in-depth understanding of the mechanism of the DLSP-S. The results are expected to offer a new perspectives and a useful guide for improving the air permeability of ultra-thick beds in iron ore sintering, contributing to industrial production.

2. Experimental Section

2.1. Materials

The sintering materials used in this study were sampled from the secondary mixture for sinter production. These sintering materials mainly consisted of iron concentrates self-produced by Ansteel of China, outsourcing fine ores and miscellaneous materials, with their proportions close to 70 wt.%, 20 wt.%, and 10 wt.%, respectively. Table 1 gives the main chemical composition of the mixed raw materials. It can be seen from Table 1 that the blend has 52.66 wt.% TFe (total Fe), 10.98 wt.% FeO, 4.15 wt.% SiO_2, 8.49 wt.% CaO, 1.42 wt.% MgO, 1.06 wt.% Al_2O_3, 10.86 wt.% LOI, and 3.38 wt.% C.

Table 1. Main chemical composition of the mixed raw materials consisting of 70% concentrates, 20% fines, and 10% miscellaneous materials (wt.%).

TFe	FeO	SiO_2	CaO	MgO	Al_2O_3	C	LOI [1]
52.66	10.98	4.15	8.49	1.42	1.06	3.38	10.86

[1] LOI: loss on ignition.

2.2. Methods

Figure 1 gives the schematic diagram of the DLSP-S. The experiments of the DLSP-S were performed in a sintering pot with dimensions of 300 mm in diameter and 1100 mm in height, as shown in Figure 2. Three S-type thermocouples from top to bottom were installed 0 mm, 350 mm, and 1000 mm beneath the top of the bed to record the temperature changes. The 1 S-type thermocouple was used for monitoring the ignition temperature, and the 2 and 3 S-type thermocouples were respectively for the sintering end temperature of the upper and the lower layer. A stand-support made of ferritic heat-resistant steel was placed vertically on the grate at the center of the sinter pot.

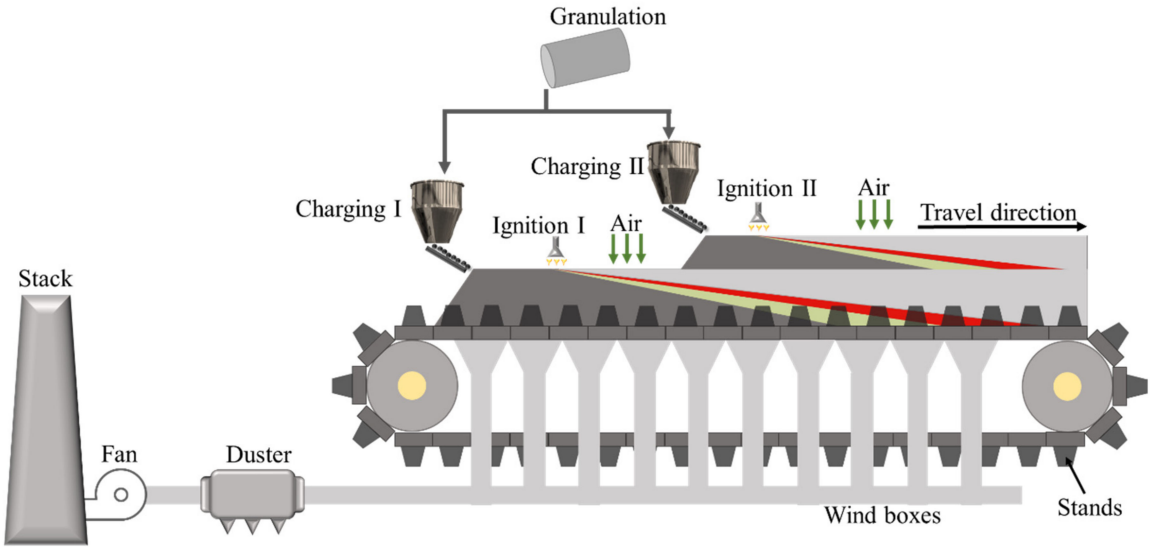

Figure 1. Schematic diagram of the double-layer sintering process with stand-support.

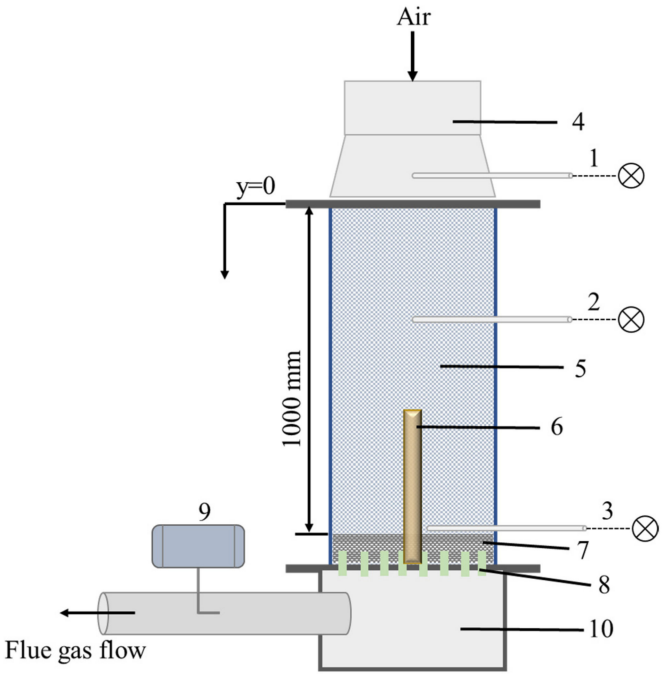

Figure 2. Schematic diagram of the sintering pot for double-layer sintering with stand-support. 1, 2, 3: S-type thermocouples; 4: hood; 5: raw mixtures; 6: stand; 7: hearth layer; 8: grates; 9: flue gas analyzer; 10: wind box.

An anemometer was used to measure the air flow through the sintering bed, and the permeability index of the sinter bed was worked out by the Voice formula of Equation (1).

$$P = \left(\frac{Q}{F}\right)\left(\frac{H}{\Delta P}\right)^{n} \quad (1)$$

where P means the permeability of the sintering bed, Q is the air flow rate passing by the sintering bed (m^3/min), F is bed section area (m^2), H is the height of the bed (mm), ΔP is the pressure drop across the bed (mmH_2O), and n is the exponent that is determined by the experiments; it is 0.6.

The traditional sintering process includes proportioning, mixing, granulation, charging, ignition, sintering, cooling, crushing, sieving, sampling, and tumbler testing [18]. The main processes of the DLSP are similar to those of the traditional sintering process. Firstly, the mixed raw materials were charged into a granulation drum (600 mm in diameter and 1400 mm in length) at 15 rpm for 5 min to granulate the fine particles into moist granules. A 1 kg amount of sinter material with a diameter of 10–16 mm was placed on the grate at the bottom of the sinter pot at a hearth layer of around 20–30 mm in height. Then, a portion of the granules was fed in as the lower layer and ignited for 1.5 min. The suction pressure of ignition and sintering was respectively controlled at 8 kPa and 10 kPa. At 9 min after the first ignition, the remaining granules were charged as the upper layer and reignited for 1 min. It should be noted that the negative pressure during the secondary ignition process was related to the air permeability of the lower layer and thus could not be controlled manually. After the cooling process, the sinter products were crushed, sieved, and sampled for subsequent detections. In this study, the height of the material bed for the upper and lower layer were respectively 350 mm (y = 0 mm to y = 350 mm) and 650 mm (y = 350 mm to y = 1000 mm). The average of the three repeated experimental data was taken as the final result.

The trials of the DLSP-S were consistent with the traditional DLSP. The difference was that before charging the lower layer, a support plate was placed vertically on the grate in the middle of the sinter pot. Two different sizes of support plates were used to vary the air permeability during the DLSP, and the specific sizes of the stands and experimental program are indicated in Table 2. Here, the double-layer sintering process with a stand height of 350 mm or 400 mm is respectively denoted as the DLSP-S_{350} or DLSP-S_{400} (the subscript number refers to a specific stand height).

Table 2. Experimental sintering scheme.

Sintering Processes	Size of Stand, mm	Moisture Content, %
DLSP	/	7.2
DLSP-S_{350}	250 × 150 × 350	7.2
DLSP-S_{400}	250 × 150 × 400	7.2

2.3. Evaluation

2.3.1. Sintering Index

Typical sintering indexes including the tumbler index (TI, %), yield (Y, %), productivity (P, $t \cdot m^{-2} \cdot h^{-1}$), and vertical sintering velocity (VSV, $mm \cdot min^{-1}$) were measured to evaluate the sinter quality of the DLSP and DLSP-S according to the reference. The final temperature at the lower layer (T_f) was defined as the highest temperature of the exhaust gas passing through the bottom of the sinter pot. Equation (2) was used to calculate the entire sintering time of the DLSP and DLSP-S t_e [16].

$$t_e = \max\{t_u + t_p, t_l\} \quad (2)$$

where t_u is the sintering time of the upper layer, min; t_p is the pre-sintering time, i.e., the sintering time of the lower feed layers before charging of the upper layer, min; t_l is the sintering time of lower layer, min.

2.3.2. Characterization

A flue gas analyzer (MGA-5, MRU, Heilbronn, Germany) was adopted to examine the concentration of O_2 in the flue gas along with the sintering process. The chemical compositions of the sinter products were analyzed by X-ray fluorescence (XRF, Axios mAX, PANalytical, Almelo, The Netherlands). The analysis of FeO in sinter products was implemented by professionals at research institutes of mining and metallurgy. The microstructure of the sinter product was characterized by an optical microscope (DMI5000 M, Leica, Wetzlar, Germany) and a scanning electron microscope (JSM-7900F, JEOL, Tokyo, Japan) equipped with an EDAX energy dispersive X-ray spectroscopy (EDS) detector (EDAX, Mahwah, NJ, USA).

3. Results and Discussion

3.1. Sinter Index of Sinter Products

Table 3 gives the influence of different stand heights on the sintering indexes. The results indicated that with stand-support sintering, the tumbler index appeared to decline, and a higher stand height predicted a greater drop, which was consistent with previous studies [19,20]. As the stand height increased from 0 mm to 350 mm, the vertical sintering velocity was significantly accelerated and the final temperature of the sinter product considerably decreased. For the DLSP-S, the load from the upper material layer was supported by the stand in the sintering bed. Therefore, a better air permeability in the lower material layer was achieved, and the flow velocity of cold air and the heat loss were accelerated, thereby leading to the decrease of the maximum temperature and the high temperature duration. It also can be seen from Table 3 that as the stand height increased from 0 mm to 350 mm, the productivity, yield, and vertical sintering velocity, respectively, increased from 1.76 $t \cdot m^{-2} \cdot h^{-1}$, 64.53%, and 22.66 $mm \cdot min^{-1}$ to 2.12 $t \cdot m^{-2} \cdot h^{-1}$, 66.74%, and 26.33 $mm \cdot min^{-1}$. Further increasing the stand height to 400 mm led to a decrease of the productivity, yield, and vertical sintering velocity. However, these are still higher than the values from the DLSP.

Table 3. Sintering indexes of double-layer sintering process with different stand heights.

Sintering Processes	TI, %	P, $t \cdot m^{-2} \cdot h^{-1}$	Y, %	VSV, $mm \cdot min^{-1}$
DLSP	59.73	1.76	64.53	22.66
DLSP-S_{350}	57.33	2.12	66.74	26.33
DLSP-S_{400}	54.40	1.95	65.48	24.90

The statistical results of the particle size distribution of the sinter products in double-layer sintering with and without a stand are displayed in Figure 3. As indicated in Figure 3, the proportion in a reasonable particle size distribution of 10–40 mm increased during the DLSP-S. In particular, the proportion in the quasi-powder grade of 5–10 mm decreased by about 2%, and the return portion of <5 mm also decreased. The DLSP-S can improve the particle size composition of the finished sinter product and reduce the content of return ore and quasi-powder.

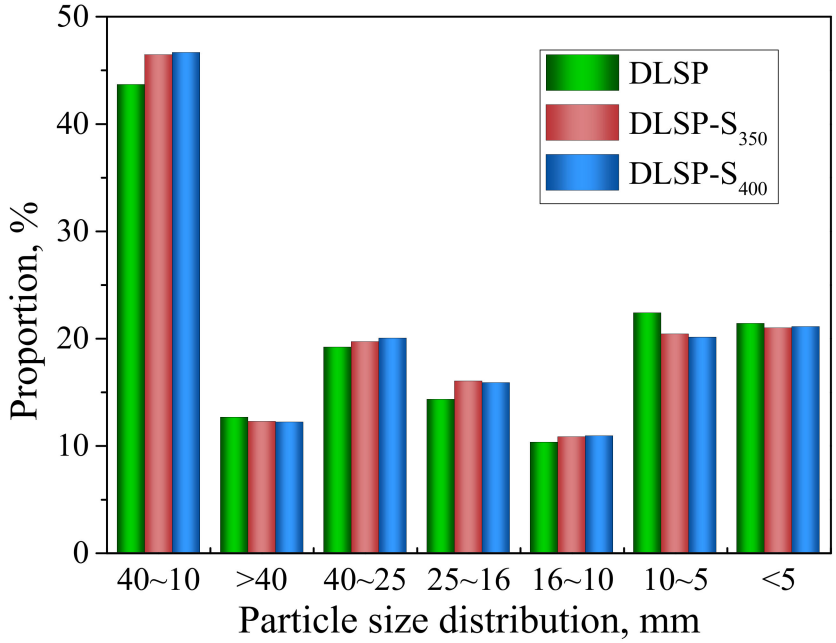

Figure 3. Particle size distribution of sinter products in the DLSP and DLSP-S.

3.2. Thermal Permeability

The variations of the bed permeability during the sintering process are shown in Figure 4. It can be clearly seen from this figure that the change of the bed permeability can be divided into three stages. Stage I indicates the first 10 min after the first charging and ignition, i.e., the monolayer sintering with a 650 mm height. In this stage, for the DLSP and DLSP-S, the permeabilities of the material layer generally increased with the progress of sintering. Compared with the DLSP, the lowest bed permeability of the DLSP-S_{350} enhanced by approximately 9.29%. When the height of the stand increased to 400 mm, the lowest permeability of the sintering bed further increased by 11.45%. Stage II is the 20 min after the second charging and ignition, i.e., the 1000 mm ultrathick double-layer sintering. As shown in Figure 4, at Stage II, the permeability of the material bed increased sharply compared with that of Stage I. Similar to Stage I, the permeability of the material layer in the DLSP-S was substantially higher than that in the DLSP. Compared with the DLSP, the lowest point of air permeability in the DLSP-S_{350} increased by 11.80%, and it further increased by 13.42% in the DLSP-S400. Stage III is the process after sintering for 30 min. At the beginning of Stage III, the sintering of the upper layer was close to the end, and thus, the permeability of the material layer dropped rapidly. When the sintering of the upper layer completed, the lower layer was still burning. At this time, the double-layer sintering converted to traditional single-layer sintering, so the permeability of the material layer was greatly improved. The lowest gas permeability at Stage III in the DLSP was 0.38, and it increased to 0.50 and 0.48 in the DLSP-S_{350} and DLSP-S_{400}, respectively, which separately increased by 31.6% and 26.3%. As a consequence, the DLSP-S can significantly improve the permeability of the material layer and help to improve the combustion environment of the lower material layer.

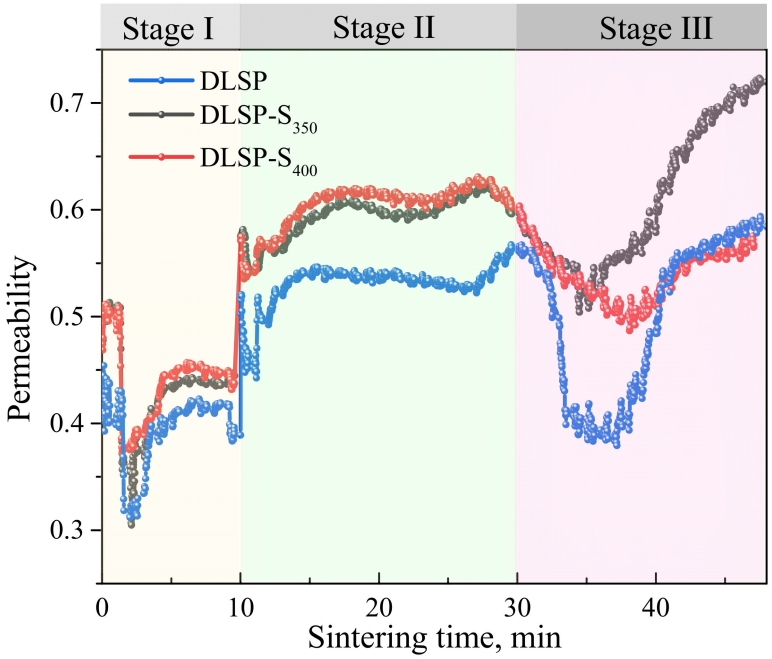

Figure 4. Permeability index of the DLSP and DLSP-S.

3.3. Flue Gas Composition

To further clarify the reasons for the improved hot air permeability, the variations in O_2 content in the sintering flue gas were measured (Figure 5). As presented in Figure 5, before the second charging and ignition (Stage I) in the DLSP, the stand height had no obvious influence on the oxygen content in the sintering exhaust gas. After the second ignition (Stages II and III), the oxygen content in the flue gas generally decreased at first and then increased, regardless of whether the stand was added. In the DLSP, the oxygen content reached the lowest amount of about 8.6% at 33 min, while in the DLSP-S, the oxygen content reached the lowest point at 28 min and increased by 2.0% to about 10.6%. Therefore, the DLSP-S can obviously increase the oxygen content in the material layer and improve the sintering atmosphere, which is conducive to the mineralization process.

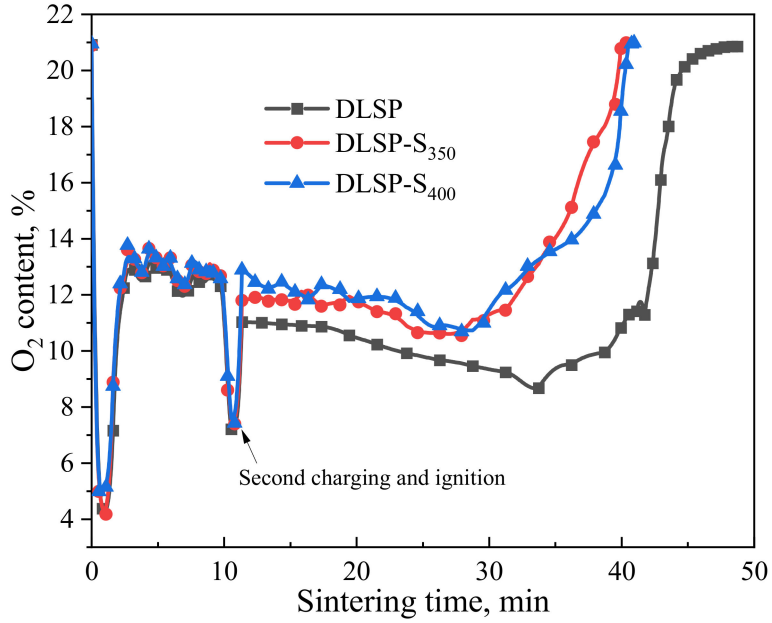

Figure 5. Content of oxygen in the flue gas of the DLSP and DLSP-S.

Table 4 shows the results of the FeO content in finished sinter products of different bed heights. At the height of 200 mm, due to the sufficient oxygen supply in the upper layer, the FeO contents of the sinter product in the DLSP and DLSP-S were almost the same. In the middle layer (height of 500 mm), the FeO contents in the sinter products of the DLSP and DLSP-S were slightly lower than at 200 mm. Due to the inadequate oxygen content at the bottom of the sintering bed in the DLSP, the FeO content in the sinter products sharply increased by 4% from the middle layer to the lower layer (height of 850 mm). During the DLSP-S, the content of FeO in the lower layer substantially decreased. When the stand height increased from 0 mm to 350 mm, the FeO content in the sinter products dropped from 11.17% to 9.62%. Due to the support effects of the stand on the upper layer of the sinter bed, the load on the lower layer could be weakened, which improved the permeability of the sintering bed.

Table 4. Content of FeO with different bed heights (%).

Distance from the Top	Upper (200 mm)	Middle (500 mm)	Lower (850 mm)
DLSP	7.75	7.17	11.17
DLSP-S_{350}	7.76	7.11	9.62
DLSP-S_{400}	7.75	7.14	9.77

3.4. Morphology Characterization

The microstructures of the sinter products from the lower layer (850 mm height from the top of the bed) of different sintering processes were characterized to further confirm the effect of the stand on the mineralization of the sinter product. Figure 6 gives the representative optical microstructure images of the sinter products of the double-layer sintering process with and without a stand. The images of Figure 6a–c display that the main mineral composition of the DLSP was magnetite (M), hematite (H), calcium ferrite (F), and silicate (S). As indicated in Figure 6a, many magnetite grains were found in the lower layer, and silicate existed between the magnetite grains. It can be found in Figure 6b that the regenerated hematite mostly appeared to be granular in shape and fish-ridge-like, and they were insufficiently linked with each other, resulting in the formation of a loose structure. Meanwhile, the corroded and lath-like calcium ferrite was interwoven with magnetite and silicate to form a mosaic structure. Furthermore, large pores existed in the sinter products (Figure 6c), all of which led to poor sinter strength in the sinter products of the DLSP.

Figure 6d–f indicates that there was more calcium ferrite and less silicate in the lower layer of the DLSP-S_{350} than that in the lower layer of the DLSP, all of which was in favor of the improvement of the sinter strength and productivity. A large number of studies [21–23] confirmed that a high oxygen atmosphere favors the formation of calcium ferrite. In addition, as shown in Figure 6d, most of the calcium ferrite occurred as acicularly shaped crystals, and a small part formed flake-shaped or column-shaped crystals. The calcium ferrite acting as the major bonding phase was intertwined with magnetite, contributing to the densification of the sinter microstructure. Hence, the sinter performance was significantly improved. From Figure 6e, it can also be seen that tabular- and granular-shaped hematite appeared and part of its solid phase was wrapped by calcium ferrite and magnetite. Prismatic or fish-ridge-shaped hematite with a low interconnection degree also formed, but its content was significantly reduced compared with the DLSP, indicating a much higher sinter strength. In Figure 6f, a melting corrosion structure of calcium ferrite and magnetite is observed. Compared with the DLSP, the porosity of the sinter products reduced, contributing to forming the close-knit micro-textures of higher sinter strength.

Figure 6g–i illustrates the microstructures of the sinter products in the lower layer of the DLSP-S_{400}. As displayed in Figure 6g,h, compared with the DLSP and DLSP-S_{350}, the thin-walled and honeycomb structures of the sinter products significantly increased. In addition, the contents of calcium ferrite and magnetite reduced because of the formation of porosity and silicate. Calcium ferrite mostly existed in striped shape, and part of it

connected with magnetite. It also can be found in Figure 6i that large areas of hematite connected with each other in a granular and loose form. The microporosity in the sinter products would seriously affect the cold strength and pulverization performance of the sinter products.

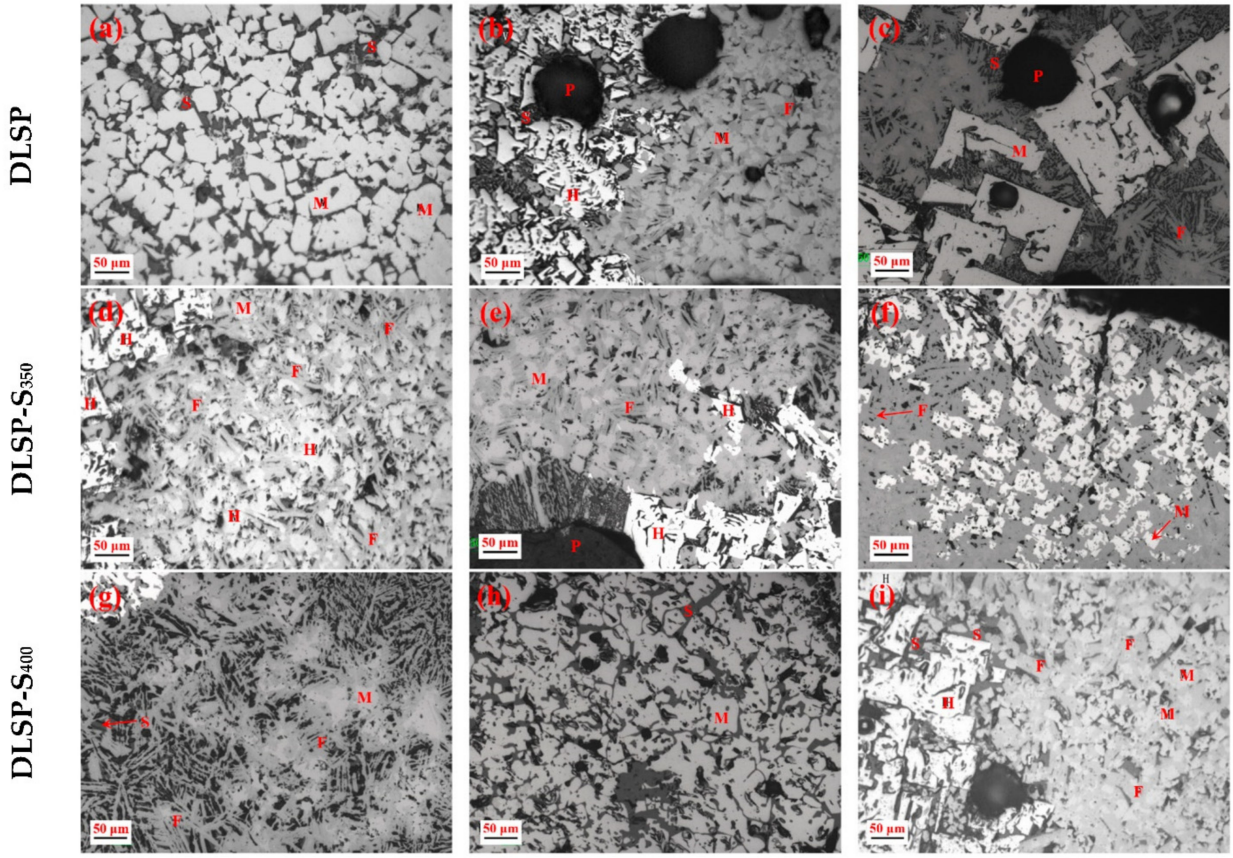

Figure 6. Microstructures of sinter products in the lower layer from different sintering processes: (**a**–**c**) DLSP; (**d**–**f**) DLSP-S_{350}; (**g**–**i**) DLSP-S_{400}. H, hematite; M, magnetite; F, calcium ferrite; S, silicate; P, pore.

4. Conclusions

1. The DLSP-S distinctly enhanced the yield and productivity of ultra-thick bed sintering, but it would also cause a certain decrease of the tumbler index. The tumbler index, yield, productivity, and vertical sintering velocity were 57.33%, 66.74%, 2.12 $t \cdot m^{-2} \cdot h^{-1}$, and 26.33 $mm \cdot min^{-1}$, respectively, at a stand height of 350 mm. The quasi-powder level of 5–10 mm and the return portion of <5 mm decreased significantly, which effectively solved the key problems existing in the practical industrial application of the DLSP;
2. Under the condition of a concentrate proportion ratio of 70%, the lowest oxygen content in the flue gas during the DLSP was about 8.6% at 33 min. The lower layer of the material bed was combusted in a low-oxygen atmosphere, thereby resulting in a poor sinter index. By using stand-support sintering, the lowest oxygen content increased to 10.6% at 28 min. The DLSP-S can significantly improve the oxygen content in the material bed, which effectively improves the combustion atmosphere and metallogenic environment of the lower layer;
3. In the DLSP, the permeability of the material layer can be divided into three stages. With the utilization of a 350 mm height stand, the lowest air permeability in Stages I–III increased by 9.29%, 11.80%, and 31.60%, respectively;

4. The morphology characterization of the sinter products demonstrated that there was more calcium ferrite in the lower layer of the DLSP-S_{350} than in the lower layer of the DLSP due to the higher air permeability, which further confirmed that the DLSP-S is beneficial to improving the quality of the sinter product. The DLSP-S was proven to be feasible in the laboratory.

Author Contributions: Conceptualization, W.G. and J.L.; methodology, Q.Z. and J.L.; software, F.W., H.Z. and L.X.; validation, L.Z., W.G. and Q.Z.; investigation, M.Z., F.W., L.X. and L.Z.; resources, M.Z., F.W. and H.Z.; writing—original draft preparation, J.L.; writing—review and editing, W.G.; supervision, Q.Z. All authors have read and agreed to the published version of the manuscript.

Funding: This research was funded by the Hunan Provincial Natural Science Foundation of China, Grant Number 2021JJ40776, and the Fundamental Research Funds for the Central Universities of Central South University, Grant Number 202044016.

Institutional Review Board Statement: Not applicable.

Informed Consent Statement: Not applicable.

Data Availability Statement: The data that support the findings of this study are available within the paper.

Conflicts of Interest: The authors declare no conflict of interest.

References

1. Wang, W.X.; Huang, J. Review of Technological Development of BF Ironmaking in China. *Iron Steel* **2007**, *42*, 2. (In Chinese)
2. Long, H.M.; Li, J.X.; Wang, P. Influence of dioxin reduction on chemical composition of sintering exhaust gas with adding urea. *J. Cent. South Univ.* **2012**, *19*, 1359–1363. [CrossRef]
3. Zhang, B. Measures for improving 900mm deep bed sintering permeability. *Sinter. Pelletizing* **2014**, *39*, 15–20. (In Chinese)
4. Wang, Y.Z.; Zhang, J.L.; Liu, Z.J.; Du, C.B. Recent advances and research status in energy conservation of iron ore sintering in China. *JOM* **2017**, *69*, 2404–2411. [CrossRef]
5. Wu, S.L.; Chen, D.F.; Zhao, C.X.; Han, H.L.; Zhang, L.H. Study on improving combustion of solid fuel in deep bed sintering. *Kang T'ieh/Iron Steel (Peking)* **2010**, *45*, 16–21.
6. Gu, F.Q.; Zhang, Y.B.; Li, G.H.; Zhong, Q.; Luo, J.; Su, Z.J.; Rao, M.J.; Peng, Z.W.; Jiang, T. Effective preparation of blast furnace burdens from superfine iron concentrates by composite agglomeration process. *J. Iron Steel Res. Int.* **2020**, *12*, 1363–1371. [CrossRef]
7. Wang, Y.Z.; Liu, Z.J.; Zhang, J.L.; Zhang, Y.P.; Niu, L.L.; Cheng, Q. Study of stand-support sintering to achieve high oxygen potential in iron ore sintering to enhance productivity and reduce CO content in exhaust gas. *J. Clean Prod.* **2020**, *252*, 119855. [CrossRef]
8. Wang, Y.Z.; Zhang, J.L.; Liu, Z.J.; Zhang, Y.P.; Liu, D.H.; Liu, Y.R. Characteristics of combustion zone and evolution of mineral phases along bed height in ore sintering. *Int. J. Min. Met. Mater.* **2017**, *24*, 1087–1095. [CrossRef]
9. Li, J.M.; Wang, M.J. Discussion and prospect on the new techniques of identical load sintering. *Iron Steel Vanadium Titan.* **1995**, *16*, 10–15. (In Chinese)
10. Higuchi, K.; Kawaguchi, T.; Kobayashi, M.; Hoso Ta Ni, Y.; Nakamura, K.; Iwamoto, K.; Fujitomo, M. Improvement of productivity by stand-support sintering in commercial sintering machines. *Rev. Métallurgie* **2002**, *99*, 241–248. [CrossRef]
11. Inazumi, T.; Fujimoto, M.; Sato, S.; Sato, K. Effect of Sinter-Cake Load Reduction by Magnetic Force on Iron Ore Sintering. *ISIJ Int.* **1995**, *35*, 372–379. [CrossRef]
12. Zuo, H.B.; Liu, Z.J.; Zhang, X.; Yang, T.J. Numerical simulation of the stand in load-reduction sintering process. *J. Univ. Sci. Technol. Beijing* **2009**, *31*, 1298–1304. (In Chinese)
13. Zuo, H.; Zhang, J.; Hu, Z.; Yang, T. Load reduction sintering for increasing productivity and decreasing fuel consumption. *Int. J. Miner. Metall. Mater.* **2013**, *20*, 131–137. [CrossRef]
14. Zuo, H.; Zhang, J.; Zhang, X.; Liu, Z.; Yang, T. Supporting structure optimization of stand in load reduction sintering process. *Chin. J. Process Eng.* **2009**, *9*, 147–151. (In Chinese)
15. Sato, S.; Kawaguchi, T.; Kato, M. Lower Limit of the Energy Consumption and the Double Ignition Process for Iron Ore Sintering. *Trans. Iron Steel Inst. Jpn.* **1988**, *28*, 705–713. [CrossRef]
16. Zhong, Q.; Li, G.H.; Liu, H.B.; Jiang, T. An efficient method for iron ore sintering with high-bed layer: Double-layer sintering. *J. Iron Steel Res. Int.* **2021**, *28*, 1366–1374. [CrossRef]
17. Zhou, M.S.; Wang, Y.D.; Han, S.F.; Zhao, D.M.; Zhu, J.W.; Zhong, Q.; Jiang, T. Research and industrial test on ultra-deep bed double-layer pre-sintering process. *Sinter. Pelletizing* **2019**, *44*, 23–38. (In Chinese)

18. Zhu, D.Q.; Xue, Y.X.; Pan, J.; Yang, C.C.; Guo, Z.Q.; Tian, H.Y.; Liao, H.; Pan, L.T.; Xuang, X.Z. An investigation into the distinctive sintering performance and consolidation mechanism of limonitic laterite ore. *Powder Technol.* **2020**, *367*, 616–631. [CrossRef]
19. Yu, W.T.; Zuo, H.B.; Zhang, J.L. Effect of stand-support area on support sintering process. *Sinter. Pelletizing* **2014**, *39*, 7–21. (In Chinese)
20. Liu, Z.J.; Wang, Y.Z.; Zhang, J.L.; Zhang, Y.P.; Zuo, H.B. Effects of stand-support on the sintering process. *Chin. J. Eng.* **2016**, *38*, 200–206. (In Chinese)
21. Webster, N.A.S.; Pownceby, M.I.; Madsen, I.C.; Kimpton, J.A. Effect of Oxygen Partial Pressure on the Formation Mechanisms of Complex Ca-rich Ferrites. *ISIJ Int.* **2013**, *53*, 774–781. [CrossRef]
22. Webster, N.A.S.; Pownceby, M.I.; Madsen, I.C.; Kimpton, J.A. Silico-ferrite of Calcium and Aluminum (SFCA) Iron Ore Sinter Bonding Phases: New Insights into Their Formation During Heating and Cooling. *Met. Mater. Trans. B* **2012**, *43*, 1344–1357. [CrossRef]
23. Webster, N.A.S.; Pownceby, M.I.; Madsen, I.C. In situ X-ray diffraction investigation of the formation mechanisms of silico-ferrite of calcium and aluminium-I-type (SFCA-I-type) complex calcium ferrites. *ISIJ Int.* **2013**, *53*, 1334–1340. [CrossRef]